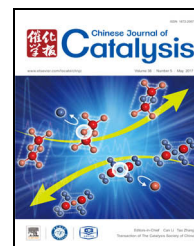


available at www.sciencedirect.comjournal homepage: www.elsevier.com/locate/chnjc

Article

Synergetic photo-epoxidation of propylene with molecular oxygen over bimetallic Au–Ag/TS-1 photocatalysts

Naixu Li^a, Bin Yang^a, Ming Liu^a, Yong Chen^a, Jiancheng Zhou^{a,b,c,*}^a School of Chemistry and Chemical Engineering, Southeast University, Nanjing 211189, Jiangsu, China^b Department of Chemical and Pharmaceutical Engineering, Southeast University Chengxian College, Nanjing 210088, Jiangsu, China^c Jiangsu Province Hi-Tech Key Laboratory for Bio-medical Research, Southeast University, Nanjing 211189, Jiangsu, China

ARTICLE INFO

Article history:

Received 2 January 2017

Accepted 1 April 2017

Published 5 May 2017

Keywords:

Gold

Silver

Titanium silicalite-1

Photocatalysis

Propene epoxidation

Synergetic effect

ABSTRACT

Au–Ag bimetallic nanoparticle-supported microporous titanium silicalite-1 catalysts were prepared via a hydrothermal-immersion method, and their structures were examined. These materials serve as efficient catalysts for the photosynthesis of propylene oxide via the epoxidation of propene. The Au/Ag mass ratio and reaction temperature were demonstrated to have significant effects on the catalytic activity and selectivity of propylene oxide. The optimal formation rate (68.3 $\mu\text{mol/g}\cdot\text{h}$) and selectivity (52.3%) toward propylene oxide were achieved with an Au:Ag mass ratio of 4:1. Notably, the strong synergistic effect between Au and Ag resulted in superior photocatalysis of the bimetallic systems compared with those of the individual systems. A probable reaction mechanism was proposed based on the theoretical and experimental results.

© 2017, Dalian Institute of Chemical Physics, Chinese Academy of Sciences.

Published by Elsevier B.V. All rights reserved.

1. Introduction

Propylene oxide (PO) is an increasingly important bulk chemical for materials containing propylene glycol and polyurethanes, which are used to produce commercial products such as adhesives, paints, and cosmetics [1]. The typical production of PO through chlorohydrin and hydroperoxidation processes is far from economically and environmentally benign [2]. Recently, numerous research activities on PO preparation over Au species from propylene and molecular oxygen have resulted in a significant advancement in the green and mild fabrication of this compound.

Suo et al. [3] reported Au-supported SiO₂ for the green conversion of propylene with dioxygen and dihydrogen to PO at 598 K and GHSV = 6000 h⁻¹. The catalytic system proved ineffi-

cient for the partial oxidation of propylene to PO because of the excessively low propylene conversion (0.9%) and selectivity to PO (17.9%) during the initial 10 min of the reaction. Jin et al. [4] achieved high selectivity toward PO (60.3%) on a 20%Ag–4%MoO₃/ZrO₂ catalyst at 673 K, 0.1 MPa, and GHSV = 7500 h⁻¹. However, the extra energy loss in the reaction, low hydrogen efficiency, and safety concern that required H₂O₂ production facilities to be limited in size rendered these approaches only temporary solutions. As a promising alternative, the direct photocatalytic gas-phase epoxidation of propylene using oxygen, similar to the direct vapor-phase epoxidation of ethylene over Ag/ α -Al₂O₃ catalysts, has gained preference among scholars. Recently, substantial efforts have been devoted to the engineering and tailoring of silica-supported metal oxides such as V₂O₅/SiO₂ [5], Nb₂O₅/SiO₂ [6], TiO₂/SiO₂ [7],

* Corresponding author. Tel: +86-25-52090621; Fax: +86-25-52090620; E-mail: jczhou@seu.edu.cn

This work was supported by the National Natural Science Foundation of China (21576050) and the Natural Science Foundation of Jiangsu Province (BK20150604).

DOI: 10.1016/S1872-2067(17)62832-8 | <http://www.sciencedirect.com/science/journal/18722067> | Chin. J. Catal., Vol. 38, No. 5, May 2017

ZnO/SiO₂ [8], MgO/SiO₂ [9], and CuO_x/SiO₂ [10] to promote the photo-epoxidation of propylene in the presence of molecular oxygen. However, studies on Ti-based materials including titanium silicalite-1, TS-2, TS- β , Ti-MCM-41, and Ti-MCM-48 [11–20] for Au chemical immobilization have demonstrated that tetrahedrally coordinated Ti is favorable for the enhanced activity and stability of Au species compared with the aforementioned materials. Both enhanced selectivity toward epoxides and stability toward C₃H₆ conversion are accessible via Au incorporation. Therefore, the catalytic materials have triggered interest among scholars searching for superior materials for the highly selective synthesis of PO via vapor-phase C₃H₆ epoxidation.

The catalytic performance of Au-based materials is strongly dependent on the particle size; only particles with sizes below 5 nm exhibit high reactivity [21–23]. However, Au particles are vulnerable to aggregation upon thermal treatment, leading to a dramatic loss of activity. It is assumed that the addition of a second metal would overcome the aggregation of the monometal [24,25] and would assist in the activation of oxygen [26,27]. The physical and chemical properties of bimetallic catalysts greatly vary depending on the composition and particle size, and these catalysts show complementary advantages and synergistic effects. Au-containing bimetallic catalysts such as Au–Cu [25,28], Au–Ag [29–34], Au–Pd [35], and Au–Pt [36] can exhibit great catalytic performance in many reactions. Among them, Ag has highly analogous cell parameters, exhibits high affinity for Au atoms, and easily forms homogeneous bimetallic Au–Ag alloys. Synergistic effects and improved activity have been achieved when using Au–Ag bimetallics for low-temperature CO oxidation [32,36]. Recently, Wittstock et al. [37,38] claimed that a nanoporous Au catalyst that was dealloyed by Au–Ag alloys exhibited high efficiency for oxidative coupling of methanol, and they confirmed that the remaining Ag could tune the availability of active oxygen and facilitate the catalytic activity.

In this study, we prepared a series of Au–Ag bimetallic nanoparticles deposited on microporous TS-1 to investigate the effect of temperature and the bimetallic composition on the catalytic activity. First, TS-1 was hydrothermally treated at 433 K for 18 h. Second, noble-metal-decorated TS-1 samples were obtained via TS-1 impregnation in precursor solutions. Subsequently, the structure and component-related information were determined using nitrogen adsorption, X-ray diffraction (XRD), Fourier-transform infrared (FTIR) spectroscopy, X-ray photoelectron spectroscopy (XPS), energy-dispersive X-ray spectroscopy (EDX), ultraviolet-visible (UV-vis) spectroscopy, photoluminescence (PL), scanning electron microscopy (SEM), and transmission electron microscopy (TEM) analyses. A comparative analysis of performance tests for an array of C₃H₆ photo-epoxidation disclosed the unique synergistic effect of these Au–Ag bimetallic catalysts. Finally, a possible reaction mechanism was proposed based on the theoretical and experimental findings.

2. Experimental

2.1. Preparation of photocatalysts

The TS-1 support was synthesized according to the procedure presented in Ref. [39]. Typically, 2 g of polyoxyethylene sorbitan monolaurate (Tween 20; s.d. KESHI) was dissolved in 32 g of distilled water (resistivity = 18.2 M Ω cm). This solution was added to a tetrapropylammonium hydroxide (TPAOH; 25% in water) solution. To the above micellar solution, 36 g of tetraethyl orthosilicate (TEOS; Aldrich) was introduced in a dropwise manner under vigorous stirring. The stirring was continued for 1 h. Next, a mixture of 1.808 g of tetra-*n*-butyl titanate (TNBT; Aldrich) and 9.12 g of isopropyl alcohol (IPA; s.d. SCR) was added to the above solution under intense agitation for 1 h. The gel solution was transferred to an autoclave and heated to 433 K for 18 h under autogenous pressure. The product was recovered by centrifugation, washed with distilled water, and dried (383 K, 12 h). The starting feedstock had the following molar composition: 0.03TiO₂:SiO₂: 0.12TPAOH: 0.009Tween20:0.88IPA:14.45H₂O. The calcination was performed in a flow of air at 823 K for 6 h.

The Au–Ag bimetallic nanoparticles supported on microporous TS-1 (denoted Au–Ag/TS-1) were prepared via an immersion method [40]. TS-1 (0.4 g) was suspended in water (20 mL) containing the required amount of 4.168 mg/mL HAuCl₄·3H₂O (purity 99.999% metal basis) and 1.25 mg/mL AgNO₃ (99.8%). The mixture was sonicated for 2 h and aged at room temperature for 24 h in the dark. Then, the solution was dried in a water bath at 353 K, calcined at 573 K for 4 h in air, and subsequently reduced in H₂ (99.999%) at 673 K for 10 h to produce the final catalyst labeled *x*Au–*y*Ag/TS-1 (*x* and *y* define the weight percentage loading of Au and Ag, respectively). TS-1 samples modified with various mass ratios of Au to Ag were prepared using the above protocol.

2.2. Characterization of photocatalysts

The N₂ sorption isotherm was measured at 77 K using a Quantachrome NovaWin analyzer. The samples were degassed at 573 K for 3 h before the measurements. The specific surface area was calculated using the Brunauer-Emmett-Teller (BET) method. The average pore diameter was determined using the Barrett-Joyner-Halenda method according to the desorption isotherm branch. The total pore volume was dependent on the absorbed N₂ volume at a relative pressure of approximately 0.98. Powder XRD patterns were obtained using a SmartLab 3 equipped with a graphite monochromator and Cu K β radiation (40 kV and 30 mA). The diffraction lines were identified by matching them with reference patterns in the JCPDS database.

TEM and EDX measurements were obtained in scanning TEM (STEM) mode using an H-600-4 electron microscope operated at an acceleration voltage of 200 kV. The catalyst powders were lightly ground and ultrasonically dispersed in ethanol at room temperature. The as-obtained solution was then dropped onto copper grids supported by holey carbon films.

XPS analysis was performed using an AXIS-Ultra-instrument (Kratos Analytical) equipped with an Al K α X-ray radiation source ($h\nu = 1486.71$ eV). A flood gun with variable electron

voltage (from 6–8 eV) was used for charge compensation. The raw data were corrected for substrate charging with the binding energy of the C 1s peak (284.6 eV). The measured spectra were fitted using the least-squares method to a product of Gaussian-Lorentzian functions after removing the background noise. The concentration of each element was calculated from the area of the corresponding peak and calibrated using the Wagner sensitivity factor.

The UV-vis diffuse reflectance spectroscopy of the as-reduced catalysts was performed on a UV-vis-near-infrared spectrophotometer (CARY5000 scan spectrophotometer), and the reduced samples were directly used for the UV-vis measurement. FT-IR spectra were collected on a TENSOR27 PMA 50 FT-IR spectrometer. The analysis of the recombination rate of charges was performed using a F-4600 FL spectrophotometer with an excitation wavelength of 260 nm.

2.3. Photocatalytic activity

Fig. 1 shows the apparatus used for the photo-epoxidation of propylene to PO. A total of 0.1 g of the photocatalysts was fed into a photoreactor, and a 100-W high-pressure mercury lamp ($\lambda = 200\text{--}600\text{ nm}$) was used as an irradiation source. The photoreactor was placed in a temperature control box in case heating was required. The reactant gases consisted of a mixture of C_3H_6 (99.99%), O_2 (99.999%), and Ar (99.999%) with a volume ratio of 1:1:19. A total gas flow of 21.2 mL/min was applied with GHSV = 6000 h^{-1} . The reactants and products were analyzed online and periodically using a gas chromatograph (GC-9850-5V) equipped with a flame ionization detector and a thermal conductivity detector. A PLOT Q column was

used to separate the propylene and oxidation products, including PO, propionaldehyde (PA), acrolein (AL), acetone (AC), acetaldehyde (AA), and ethanol (EtOH). However, a carbon molecular sieve (60–80) was used to separate O_2 and CO_2 . The standard definition of conversion was not used in this study. In our study, the conversions were low, in the range of 0.01–1.00%. To accurately quantify the conversions in the photo-epoxidation, we defined the C_3H_6 conversion as the sum of all the products converted to C_3 . The PO formation rate, C_3H_6 conversion rate, and product selectivity were expressed as follows [41]:

$$\text{PO formation rate} = \text{Concentration of the product detected on stream} \times \text{flow rate/weight of the photocatalysts} \quad (1)$$

$$\text{C}_3\text{H}_6 \text{ conv. rate} = \sum \text{Rate of all products converted to C}_3 \quad (2)$$

$$\text{Product selectivity} = (\text{Product converted to C}_3 / \text{all products converted to C}_3) \times 100\% \quad (3)$$

3. Results and discussion

3.1. Characterization of photocatalysts

3.1.1. Physical properties

Table 1 lists the BET surface areas, average pore sizes, and pore volumes of the catalysts. The BET surface areas (470–528 m^2/g) gradually decreased with increasing Ag content in the bimetal loading, indicating that the pores in TS-1 may have been clogged by the metal. However, Au–Ag/TS-1(4/1) had a larger specific surface area than TS-1, which suggests that the noble metal was well dispersed on the support and that the channels were not plugged. The bimetallic particle size also showed the same increasing trend (from 2.1 to 4.2 nm) with

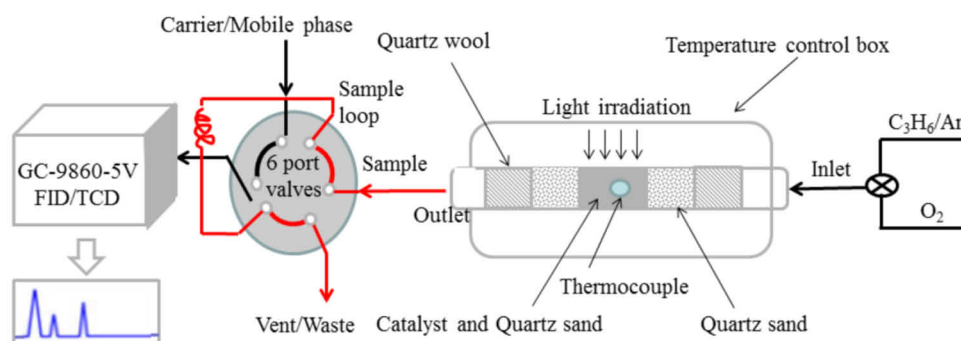


Fig. 1. Apparatus for gas-phase photocatalytic epoxidation of propylene.

Table 1

Chemical composition and textural properties of catalysts and estimated metal particle sizes.

No.	Photocatalyst (wt%)	Au/Ag mass ratio ^a	Pore size (nm)	Pore volume ^b (cm^3/g)	BET surface area (m^2/g)	Metal particle size ^c (nm)
1	TS-1	–	1.34	0.289	519	–
2	0.1Au/TS-1	1:0	1.20	0.267	477	2.1
3	0.1Au–0.025Ag/TS-1	4.15:1	1.35	0.290	528	2.4
4	0.1Au–0.1Ag/TS-1	1.21:1	1.35	0.307	472	2.9
5	0.1Au–0.15Ag/TS-1	2.13:3.15	1.34	0.311	470	3.2
6	0.15Ag/TS-1	0:1	1.33	0.270	463	4.2

^aAu/Ag mass ratio determined by EDX.

^bTotal pore volume obtained from $p/p_0 = 0.98$.

^cParticle size measured by TEM.

increasing Ag content. In addition, the metal loading did not have a substantial effect on the pore size or volume of TS-1. The Au/Ag nominal mass ratios were consistent with the compositions measured using EDX.

3.1.2. XRD analysis

The structures of the as-prepared catalytic materials were confirmed by XRD. Fig. 2(a) shows diffraction lines at $2\theta = 7.8^\circ$, 8.8° , 23.2° , 23.8° , and 24.5° , representing the indices of the (101), (200), (501), (151), and (313) lattice planes, respectively. The perfect match of these peaks with the standard peaks of the TS-1 curve (JCPDS card no. 70-4276) indicates that the orthorhombic phase and MFI structure of the sample [42–44]. The incorporation of Ti^{IV} into the framework is indicated by the change from monoclinic symmetry (S-1) to orthorhombic symmetry (TS-1) by virtue of the disappearance of the peak split at $2\theta = 24.5^\circ$ and 29.5° [44]. In addition, for the Au–Ag/TS-1 samples, the perfect coincidence of the shapes and positions of the characteristic peaks with those associated with TS-1 indicates that the metal loading is independent of the latter framework. Nevertheless, diffraction lines attributable to Au and Ag are hardly observed in Fig. 2(b) because of their exces-

sively low loading (≤ 0.25 wt%) or high dispersion on the TS-1 surface.

3.1.3. UV-vis spectra

The UV-vis spectra in Fig. 3(a) reveal one strong absorption edge at 214 nm. This band is attributed to electronic transitions between O^{2-} and Ti^{4+} in the isolated framework Ti^{IV} centers in a tetrahedral environment. The absence of an absorption band at 320–400 nm confirms that neither anatase nor extraframework Ti was present in these samples [45]. It is apparent that the absorbance is closely connected with the metal loading. For the monometallic loading, Ag/TS-1 exhibits high intensity compared with Au/TS-1, which may be related to its physical and chemical properties. Compared with Au, Ag shows a greater tendency to conduct photogenerated charges [46]. For the Au/Ag bimetallic catalysts, the absorbance deviated from that of its counterpart with increasing Ag amount. This phenomenon is possibly connected to the bimetallic composition and particle size [21–23]. Similar to the Au/Ag (4/1) bimetallic catalyst, the particle size was small and well dispersed on the support, which is favorable for the transfer of photogenerated charges. Therefore, the small addition of Ag to Au is beneficial

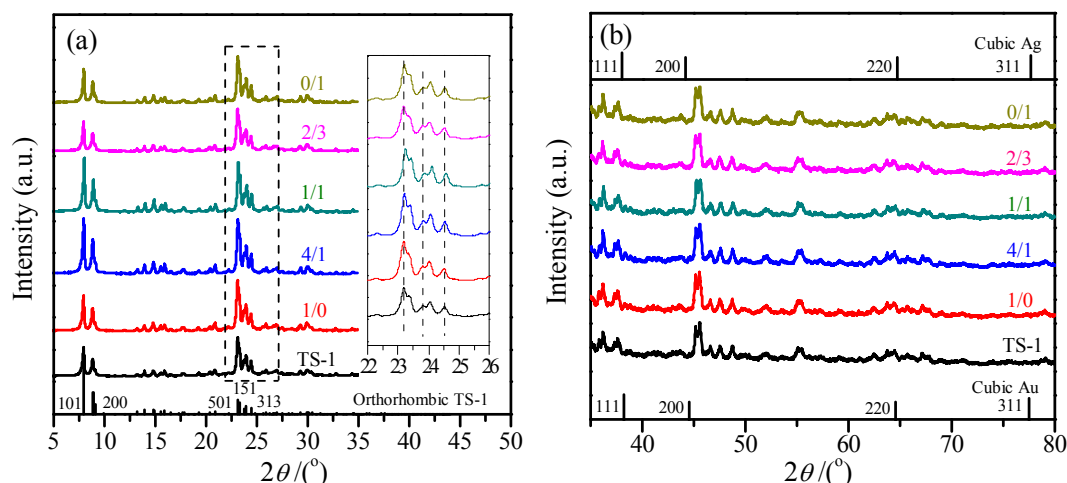


Fig. 2. XRD patterns of catalysts with different Au/Ag mass ratios. (a) $2\theta = 5^\circ$ – 35° ; (b) $2\theta = 35^\circ$ – 80° .

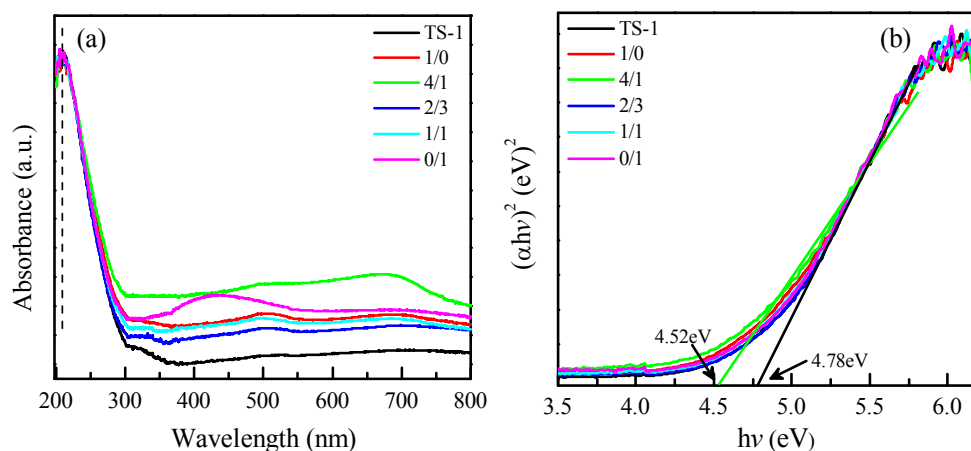


Fig. 3. UV-vis absorption spectra (a) and plot of $(\alpha hv)^2$ vs. $h\nu$ (b) for the direct optical band gap of Au–Ag/TS-1 with different Au/Ag mass ratios.

for the photocatalytic reaction. Our results provide evidence of the close connection between the interfaces at the nanoscale level, leading to the formation of a surface heterojunction, which could affect its electron transfer. The band gap of the catalysts can be calculated using the following empirical formula:

$$\alpha h\nu = A(h\nu - E_g)^{1/2}$$

where α , ν , h , E_g , and A are the absorption coefficient, light frequency, Planck constant, bandgap energy, and proportionality constant, respectively. The band gap energies of TS-1 and Au–Ag/TS-1 are shown in the Fig. 3(b). E_g of pure TS-1 was estimated to be 4.78 eV, and after the bimetal loading, the absorption edge exhibited a red shift, extending the E_g of Au–Ag/TS-1(4/1) to 4.52 eV. This result indicates that the absorption intensity of TS-1 in the region of UV light can be increased by bimetal loading, which may be explained by the surface plasmon resonance effect of the metal.

3.1.4. FTIR spectra

To further understand the structure of TS-1, FTIR spectra were obtained. The major peaks at 1220, 1100, 800, 550, and 450 cm^{-1} are consistent with those of the MFI topology structures. Next, in all cases, the peak centered at 960 cm^{-1} suggests the incorporation of Ti into the framework [47–50], as observed in Fig. 4. Moreover, modification of TS-1 with noble metals did not result in variation of the shape or mode of the FTIR curve, implying an untouched structure before and after Au and Ag loading.

3.1.5. PL spectra

PL spectra serve as indicators of the recombination rate of photogenerated excitons, which provides deeper insight into photocatalytic processes. The PL spectra of pure TS-1 and TS-1 containing different Au/Ag mass ratios contained the same fluorescence peaks with an excited wavelength of 260 nm (Fig. 5). It is assumed that a photocatalyst will generate electrons and holes under light excitation and that the recombination of electrons and holes will emit fluorescence. A low fluorescence emission intensity indicates a low recombination rate of elec-

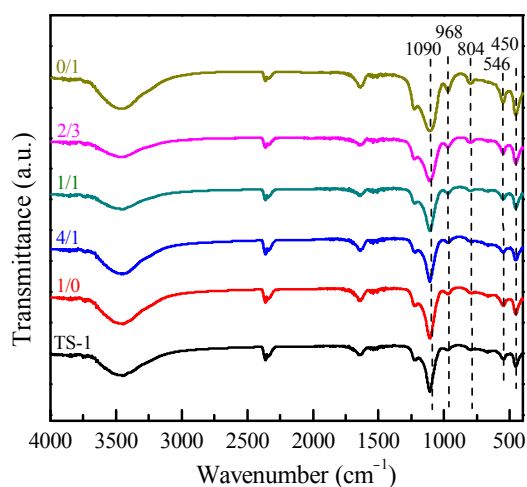


Fig. 4. FTIR spectra of Au–Ag/TS-1 with different Au/Ag mass ratios.

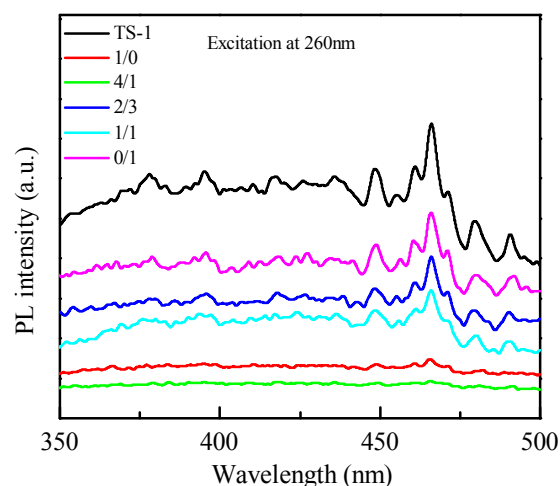


Fig. 5. PL spectra of Au–Ag/TS-1 with different Au/Ag mass ratios at an excitation wavelength of 260 nm.

trons and holes, which translates into a high photocatalytic activity. In our photocatalytic system, the fluorescence intensity decreased with increasing metal loading, which may be explained by the electron transfer from TS-1 to the metal and the recombination of photogenerated electrons and holes being inhibited under UV-light irradiation. For monometallic loading, Ag/TS-1 showed high intensity compared with Au/TS-1. However, with increasing Au content in the Au/Ag bimetallic catalysts, the fluorescence intensity gradually decreased, demonstrating that Au/Ag-loaded on TS-1 provided better ability to deliver electrons and inhibited the recombination of photoinduced charges and holes on the Au/Ag-loaded TS-1 surface. Among the bimetallic catalysts, Au/Ag (4/1) exhibited the lowest intensity, which indicates it demonstrated the best separation effect for the photocatalytic reaction. This phenomenon is consistent with the catalytic activity findings.

3.1.6. SEM and TEM analyses

For propylene epoxidation catalyzed by metal nanoparticles, the size of the nanoparticle is an important factor. The particle size and distribution of the Au–Ag bimetallic catalysts were determined using SEM and high-resolution TEM. Figs. 6(a) and 7(a) display uniform, isolated, and smooth-surface TS-1 microspheres with a narrow size distribution of 0.4–0.5 μm . Fig. 6(b) reveals the lattice spacing of 1.003 nm indexed as the (200) planes of TS-1. The metal nanoparticle size is of the first magnitude for elevated catalytic behavior of propene oxidation. High-resolution TEM (HRTEM) images of TS-1 modified with different mass ratios of Au/Ag are presented in Fig. 9. The diffraction lines of Au–Ag bimetal are similar to those of monometallic nanoparticles because of their similar lattice constants (0.408 vs. 0.409 nm) and the face-centered-cubic structures of Au and Ag. Thus, the HRTEM image of Au–Ag/TS-1(4/1) in Fig. 6(c) reveals lattice spacings of 0.236, 0.204, and 0.143 nm indexed as the (111), (200), and (220) planes of Au–Ag bimetal, respectively. Fig. 6(d) presents an image and EDX pattern of Au–Ag/TS-1(4/1). The sample was a pink powder, with Ti, O, and Si elements clearly detected in Fig. 6(d). The loadings of Au and Ag were small; therefore, Au and Ag are not easily detected

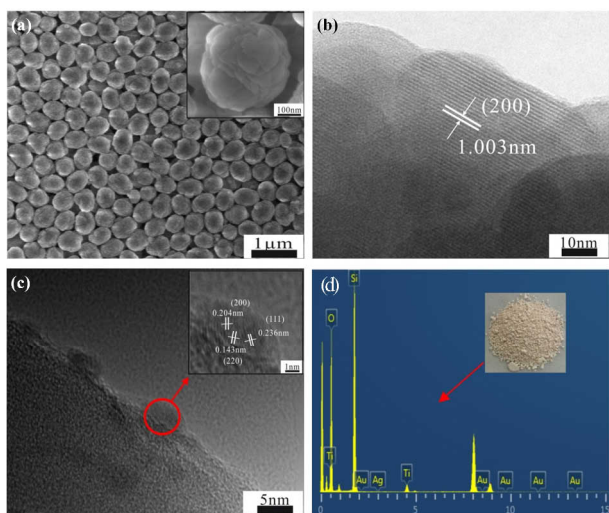


Fig. 6. SEM (a) and HRTEM (b) image of TS-1; HRTEM image (c) and EDX pattern (d) and image (inset) of Au-Ag/TS-1(4/1).

in Fig. 6(d). However, these metals can be clearly observed in the elemental EDX mapping (Fig. 8). The metal particle size and size distribution for the Au-Ag bimetallic catalysts are presented in Fig. 7. The particle size of the Au-Ag bimetallic catalysts was much larger than that of Au/TS-1. The samples with Au/Ag mass ratios of 4:1, 1:1, 2:3, and 0:1 had average particle sizes of approximately 2.4, 2.9, 3.2, and 4.2 nm, respectively. With increasing Ag content, the particle size increased, which is attributed to the interaction between Au and Ag. The nanoscale

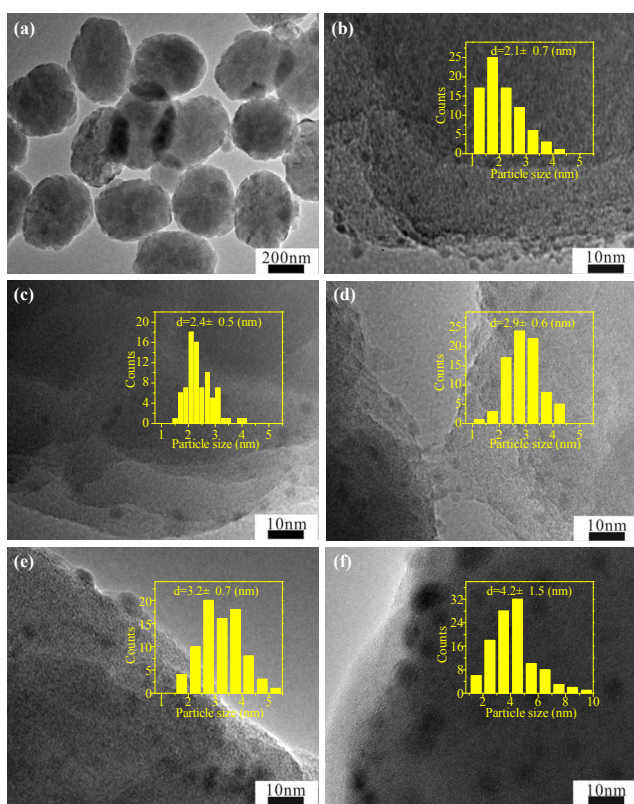


Fig. 7. Particle size and size histograms for TS-1 (a) and Au/Ag-modified TS-1 for Au/Ag mass ratios of 1/0 (b), 4/1 (c), 1/1 (d), 2/3 (e), and 0/1 (f).

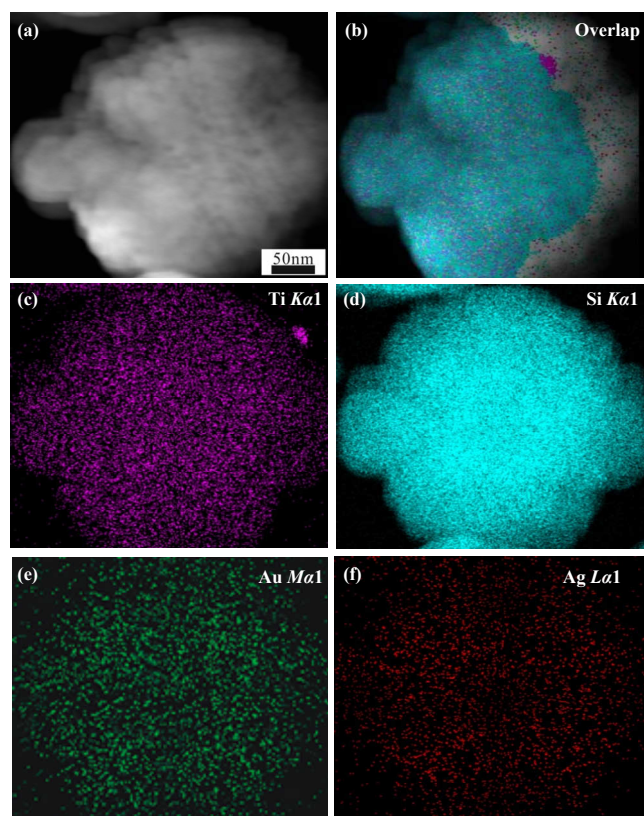


Fig. 8. (a) STEM image of Au/Ag (4/1) catalyst, (b) overlapping elemental intensities, and (c–f) measured (c) Ti K, (d) Si K, (e) Au M, and (f) Ag L intensities for the corresponding EDX mappings of Au/Ag (4/1) catalyst in the region shown in (a).

elemental EDX mapping of the Au/Ag (4/1) catalyst (Fig. 8) reveals that most of the Ag species were distributed in the Au domain and were clearly distinguishable. The Si and Ti species were equidistributed, and the Au and Ag species overlapped in the Au-Ag/TS-1 catalysts. The close integration of Au and Ag may be the origin of the synergistic effect.

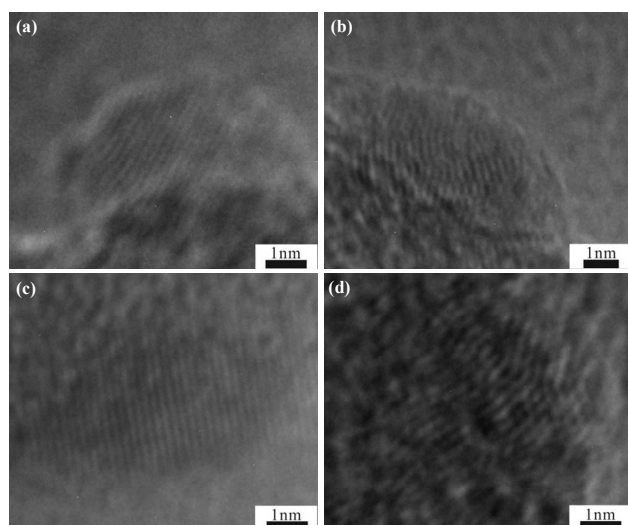


Fig. 9. HRTEM images of Au/Ag-modified TS-1 for the following Au/Ag mass ratios. (a) 1/0; (b) 4/1; (c) 1/1; (d) 2/3.

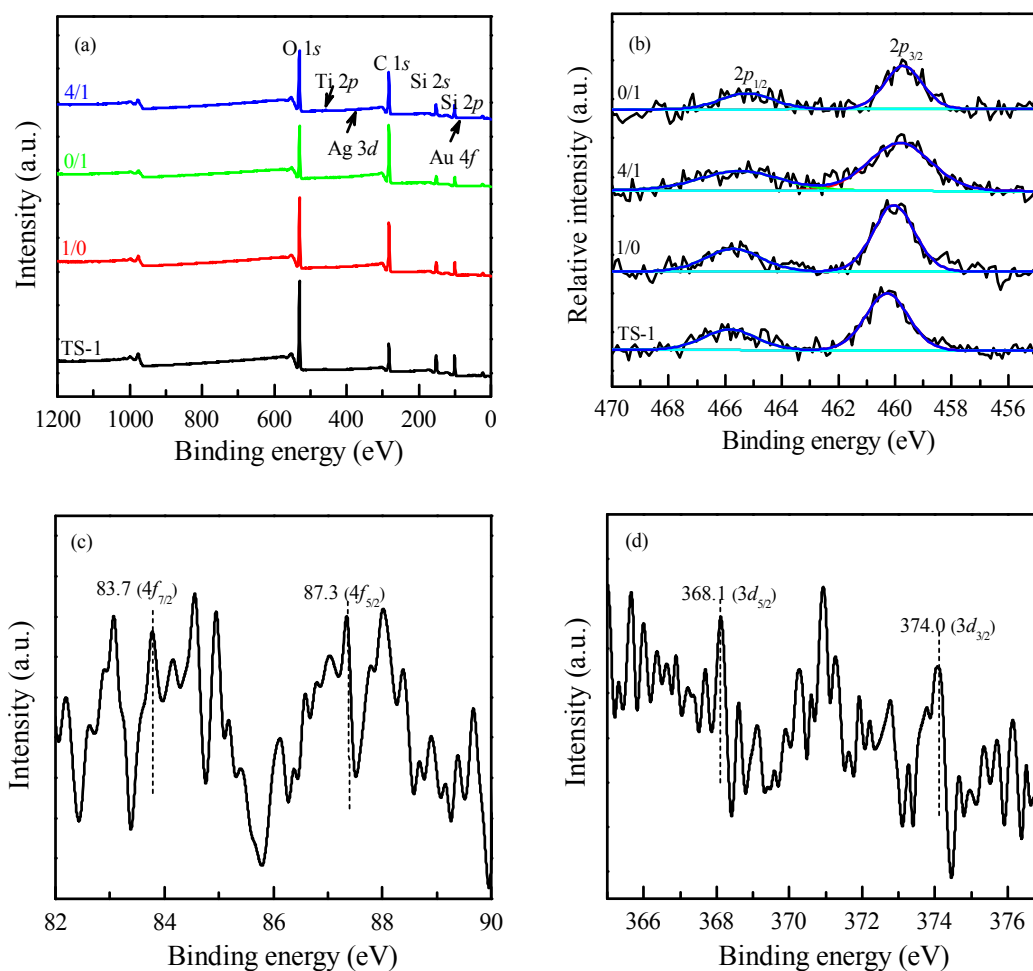


Fig. 10. XPS spectra. (a) Survey spectrum; (b) Ti 2p; (c) Au 4f; Au/Ag = 1/0; (d) Ag 3d; Au/Ag = 0/1.

3.1.7. XPS spectra

To further investigate the element state and interaction between metal nanoparticles and TS-1, XPS spectra were obtained, and the results are presented in Fig. 10. O, Ti, Si, C, Au, and Ag were detected in TS-1 and TS-1 with different Au/Ag mass ratios (1/0, 4/1, 0/1) catalysts, as shown in Fig. 10(a). The binding energies of Ti 2p are presented in Fig. 10(b) for the above catalysts, and the peaks at 460 and 465.8 eV were well defined for TS-1. The peak at 460 eV is usually attributed to Ti in tetrahedral coordination [51]. With the metal loading, the binding energy of Ti $2p_{3/2}$ shifted down by 0.4 and 0.5 eV for Au/Ag mass ratios of 4/1 and 0/1, respectively, which is explained by the greater tendency of Ag to conduct electrons between a metal and support because of its low work function. The work function of Ag (4.26 eV) is lower than that of the support (4.78 eV); therefore, the electrons have the tendency to aggregate on the support, which leads to the decrease of the binding energy. For the Au–Ag bimetal, Au has a higher work function (5.1 eV), which inhibits electron transfer; therefore, the shift decreases compared with that of monometallic Ag. This phenomenon indicates the generation of a new surface of Ti metal, which promotes electron transfer and is favorable for

photocatalytic propene epoxidation. Fig. 10 (c) shows the theoretical binding energies of Au $4f_{7/2}$ and $4f_{5/2}$ for Au/TS-1. The theoretical binding energies of Ag $3d_{5/2}$ and $3d_{3/2}$ for Ag/TS-1 are shown in Fig. 10(d). The peak intensities for Au and Ag were near the background because of the small loadings of Au and Ag. It is difficult to clarify the forms of Au and Ag because of their small loadings. They may be assumed to be present in metal form because Au and Ag are more easily reduced in bimetallic catalysts under hydrogen [52].

3.2. Photo-epoxidation of propylene to PO

Typically, it takes 2–3 h to reach a steady state. To distinguish the thermal effect from the photocatalytic process, an epoxidation experiment was performed over TS-1 under different lighting conditions (with and without UV light). No activity was observed with UV illumination, as demonstrated by the results in Table 2. Therefore, the epoxidation over the catalyst was clearly photocatalytic epoxidation. In addition, with metal loading, PO and CO_2 were not detected at the different temperatures without UV illumination. Table 3 summarizes the results of the photocatalytic epoxidation of propylene with oxygen over various samples in a continuous packed-bed reactor at

Table 2PO formation rates ($\mu\text{mol}/(\text{g}\cdot\text{h})$) over TS-1 for various lighting conditions and temperatures.

Temperature (K)	323	343	363	383	403	423	443	453	463	473
UV-light	37.5	40.4	42.3	44.0	47.9	50.5	52.5	53.5	52.7	50.9
No UV-light	ND									

ND: not detected by gas chromatography.

various temperatures with UV light excitation. The formation rate of PO ranged from 37.5 to 68.3 $\mu\text{mol}/\text{g}\cdot\text{h}$ and the PO selectivity ranged from 16.5% to 53.0%. In addition to PO, AA was detected as major by-product and AL, PA, AC, and EtOH were detected as minor by-products. Interestingly, Fig. 11(a) reveals that the bimetallic catalyst with an Au/Ag mass ratio of 4:1 showed the best activity and demonstrated a collaborative effect for propylene epoxidation compared with the catalyst with monometallic loading. When the Au/Ag mass ratio was increased from 4:1 to 1:0 or decreased from 4:1 to 1:1 or 2:3, the activity decreased. This phenomenon may be attributed to the metal particle size and bimetallic composition. For the bimetallics, 4/1(Au/Ag) had the smallest particle size and provided the largest specific surface area, which are beneficial for reactant adsorption. In addition, with the incorporation of a small

amount of Ag, 4/1(Au/Ag) exhibited better electron transfer and an improved separation effect for photogenerated electrons and holes. Monometallic Ag exhibited a larger particle size (Table 1), which is unfavorable for this reaction. Although Au particles are small, electron transfer from the metal to adsorbate is difficult because of the high work function of Au. Detailed explanations are provided below.

3.2.1. Effect of reaction temperature on photo-epoxidation activity

Monotonic relationships were not observed for any of the photocatalysts between the reaction temperature and the PO formation rate or C_3H_6 conversion rate, as observed in Fig. 11. Instead, the activity first increased with increasing temperature (up to 443 K) and then decreased from 443–473 K. The photo-

Table 3

Selectivities for photo-epoxidation over Au–Ag/TS-1 for photocatalysts with various Au/Ag mass ratios at various temperatures.

Entry	Catalyst	Temperature (K)	C_3H_6 conversion rate ($\mu\text{mol}/(\text{g}\cdot\text{h})$)	PO formation rate ($\mu\text{mol}/(\text{g}\cdot\text{h})$)	Selectivity (%)					
					AA	EtOH	PO	AL	PA	AC
1	TS-1	323	72.1	37.5	48.0	trace	52.0	trace	ND	ND
		343	168.3	40.4	22.8	20.3	24.0	16.5	ND	16.3
		363	215.3	42.3	20.8	16.7	20.6	13.9	13.4	14.6
		383	249.1	44.0	27.8	14.2	18.4	13.8	13.5	12.3
		403	266.7	47.9	32.4	12.7	18.3	13.7	12.1	10.8
		423	279.4	50.5	33.4	11.8	18.1	13.6	13.0	10.1
		443	296.6	52.5	34.2	11.3	17.7	13.3	13.6	9.9
		453	295.7	53.5	34.9	10.7	17.5	13.9	13.7	9.3
		463	290.3	52.7	34.7	10.7	17.2	14.1	13.9	9.4
		473	288.7	50.9	33.7	10.5	16.7	14.5	15.4	9.2
2	Au/Ag (1/0)	323	71.9	37.8	47.4	trace	52.6	trace	ND	ND
		343	170.3	40.9	23.7	19.4	24.7	16.8	ND	15.4
		363	220.2	48.4	28.2	18.6	22.0	16.1	ND	15.1
		383	264.0	53.6	31.6	12.5	20.3	13.9	11.1	10.5
		403	291.7	59.8	32.6	12.0	20.5	13.8	11.4	9.7
		423	304.8	62.6	32.8	11.5	20.5	13.8	11.9	9.5
		443	310.5	64.9	32.6	10.7	20.9	14.3	12.4	9.1
		453	306.3	62.8	32.4	10.6	20.5	14.8	12.6	9.1
		463	304.4	61.2	31.5	10.8	20.1	15.1	13.6	8.9
		473	302.5	59.0	31.3	10.3	19.5	15.4	14.8	8.7
3	Au/Ag (4/1)	323	74.1	38.8	47.7	trace	52.3	trace	ND	ND
		343	172.5	41.4	23.2	20.1	24.0	16.4	ND	16.3
		363	237.6	50.1	21.8	15.9	21.1	14.3	13.4	13.5
		383	294.6	60.4	33.2	11.3	20.5	14.2	10.9	9.9
		403	315.0	64.9	33.7	10.6	20.6	14.1	11.5	9.5
		423	327.5	67.8	34.3	10.1	20.7	14.0	11.6	9.3
		443	333.1	68.3	34.3	9.9	20.5	14.2	12.2	8.9
		453	349.7	66.1	34.3	9.8	18.9	14.7	13.4	8.8
		463	341.3	63.5	33.5	10.0	18.6	15.0	14.1	8.7
		473	339.3	60.4	32.7	10.0	17.8	15.8	14.9	8.7

(To be continued)

Table 3 (continued)

Entry	Catalyst	Temperature (K)	C ₃ H ₆ conversion rate (μmol/(g·h))	PO formation rate (μmol/(g·h))	Selectivity (%)					
					AA	EtOH	PO	AL	PA	AC
4	Au/Ag (2/3)	323	71.2	37.6	trace	trace	52.8	trace	trace	trace
		343	151.8	40.7	23.2	19.4	26.8	16.0	ND	14.6
		363	210.2	44.5	23.2	15.1	21.1	14.2	13.2	13.2
		383	245.6	52.3	29.6	13.3	20.5	13.5	11.7	11.4
		403	263.2	54.5	30.6	13.0	20.7	13.5	11.7	10.5
		423	272.5	56.7	31.0	12.4	20.8	13.5	12.0	10.3
		443	273.8	57.5	30.6	12.2	21.0	13.7	12.4	10.1
		453	270.1	57.2	30.4	12.1	21.1	14.3	12.2	9.9
		463	267.6	56.2	30.0	12.1	21.0	14.6	12.4	9.9
		473	270.9	54.1	29.7	12.2	20.5	15.1	12.5	10.0
5	Au/Ag (1/1)	323	71.3	37.8	47.0	trace	53.0	trace	ND	ND
		343	131.4	40.5	28.5	trace	30.8	21.3	ND	19.4
		363	196.1	45.7	30.1	trace	23.3	16.9	15.7	14.0
		383	260.3	52.6	31.0	12.6	19.6	14.6	11.4	10.8
		403	283.4	56.4	31.4	12.7	19.9	13.7	12.2	10.6
		423	301.1	59.6	33.0	11.4	19.8	13.5	12.7	9.6
		443	297.5	60.4	33.1	11.0	20.3	13.7	12.4	9.5
		453	298.5	59.8	32.7	11.0	20.3	14.0	12.5	9.4
		463	293.4	58.7	32.2	11.0	20.0	14.3	13.2	9.3
		473	289.8	55.1	31.4	11.5	19.0	14.8	13.6	9.7
6	Au/Ag (0/1)	323	71.5	37.6	47.4	trace	52.6	trace	ND	ND
		343	135.3	40.6	29.0	trace	30.0	21.1	ND	19.9
		363	205.6	44.0	29.4	trace	21.4	17.3	16.3	15.6
		383	238.1	48.1	29.4	13.1	20.2	14.2	11.9	11.2
		403	261.3	52.8	30.7	12.7	20.2	13.9	12.1	10.4
		423	272.2	55.0	31.3	12.4	20.2	13.7	12.2	10.2
		443	271.4	56.2	31.0	11.9	20.7	14.1	12.4	9.9
		453	269.9	55.2	30.4	11.9	20.3	14.4	13.0	10.0
		463	266.0	54.0	30.0	12.0	20.0	14.7	13.4	9.9
		473	268.9	51.9	29.7	12.0	19.3	15.0	14.1	9.9

ND: not detected by gas chromatography.

AA: acetaldehyde; EtOH: ethanol; PO: propylene oxide; AL: acrolein; PA: propionaldehyde; AC: acetone.

reaction is often a light-driven rather than a thermally induced process. Kim et al. [53] reported that the true activation energy is nil in a photoreaction. Therefore, the activation energy is the apparent activation energy, which is very small. Hence, desorption of the final product and reactant adsorption will become important factors for this reaction. Desorption and adsorption are endothermic and exothermic processes, respectively. In

other words, increasing the temperature favors desorption of the photocatalytic reaction products, which enhances the reaction efficiency by releasing more active sites for reaction. However, increasing the temperature may suppress propylene adsorption on photocatalysts, which may reduce the reaction efficiency. Therefore, the reaction temperature has competing effects on the reaction rate in this study. During the

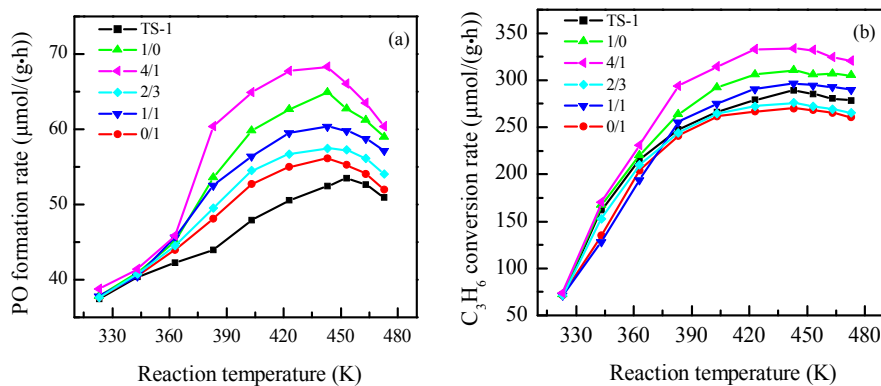


Fig. 11. Correlation between reaction temperature and PO formation rate (a) and C₃H₆ consumption rate (b) for photocatalysts with various Au/Ag mass ratios.

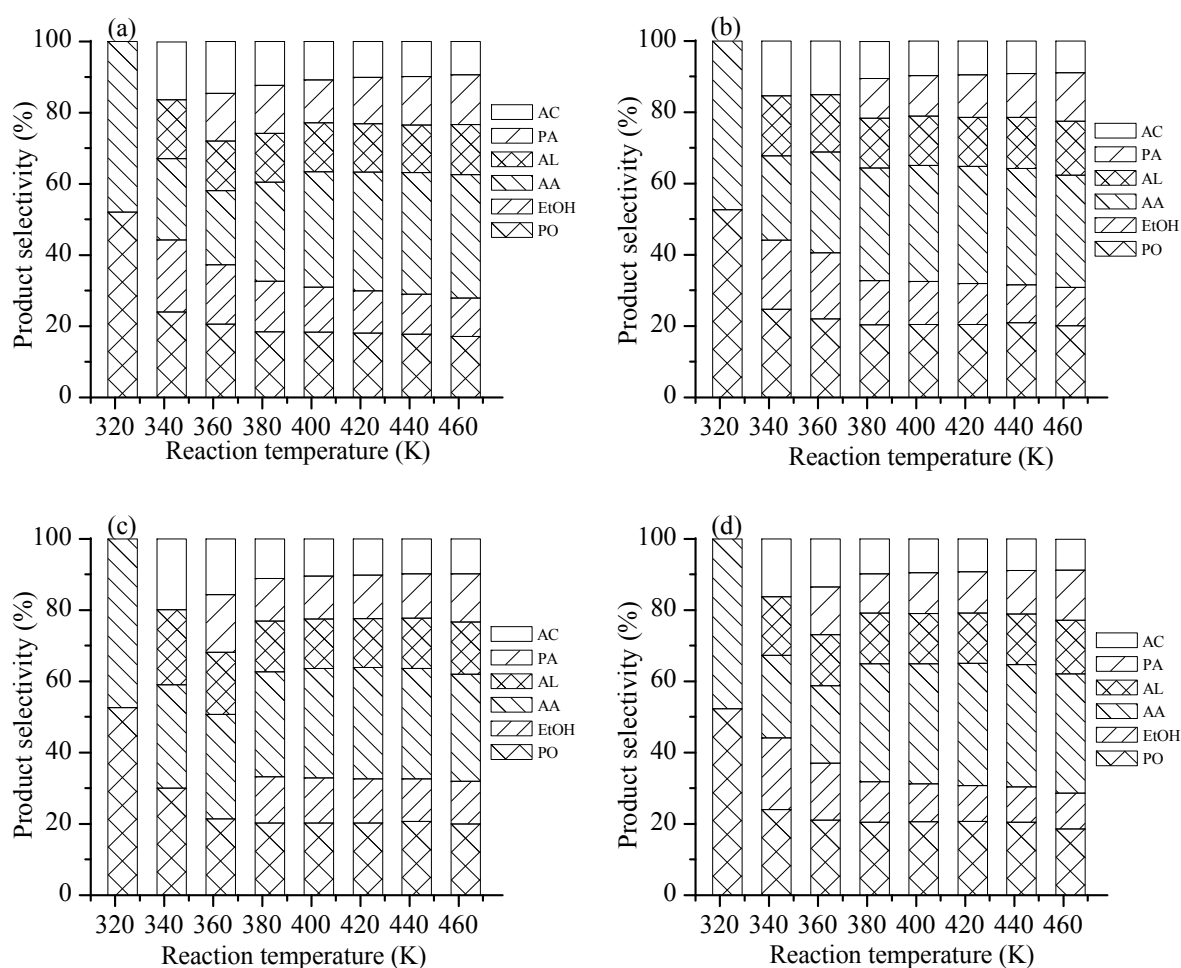


Fig. 12. Correlation between reaction temperature and product selectivity for TS-1 (a) and TS-1 modified with Au/Ag mass ratios of 1/0 (b), 0/1 (c), and 4/1 (d).

low-temperature period, propylene adsorption is dominant, and the product desorption rate increases with increasing temperature; therefore, the PO formation rate monotonically increases. However, when the temperature increases above 412 K, product adsorption is the rate-determining step, and high temperature is unfavorable for propylene adsorption. Therefore, the PO formation rate decreases with increasing temperature. Fig. 11(a) demonstrates that the Au-Ag/TS-1(4/1) catalyst at 443 K exhibits an optimal PO formation rate of 68.3 $\mu\text{mol/g}\cdot\text{h}$. Fig. 12 shows the product distribution for various temperatures for TS-1 and TS-1 modified with Au/Ag mass ratios of 1/0, 0/1, and 4/1. High temperature led to low PO selectivity and high selectivity to the by-products, which may be attributed to the competition of multiple reactions toward different products. Nguyen et al. [54] reported that high temperature inhibits the formation of hydroxyl radical $\text{OH}^*(\text{ads})$ intermediates, which are generated from water molecules. Therefore, high temperature will restrain the conversion of PA into propionic acid ($\text{C}_2\text{H}_5\text{COOH}$), the intermediate product of EtOH, resulting in an increase of PA and decrease of EtOH with increasing temperature. These researchers also

noted that heating may increase not only the desorption of photocatalytic products but also the partial oxidation and/or total oxidation of the intermediates. Therefore, the product distribution would be rearranged.

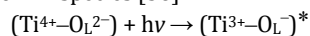
3.2.2. Effect of Au/Ag loading on photo-epoxidation

Fig. 11 reveals that loading with the monometal or bimetal resulted in similar activity and selectivity as those of TS-1 at low temperature (from 323 to 343 K). Above 343 K, loading with the monometal or bimetal greatly increased the PO formation rates. This phenomenon may be connected with reactant adsorption, product desorption, and photon utilization. Low temperature is beneficial for reactant adsorption but unfavorable for product desorption, which inhibits the reaction efficiency by occupying more active sites for the reaction [54]. Although the introduction of Ag to Au will affect its physical and chemical properties, which is beneficial for photo-epoxidation by improving the oxygen adsorption, activation, and electron transfer [26,27,46], photogenerated electron utilization is suppressed because of the limited active sites. Therefore, during the low-temperature period, loading with the

monometal or bimetal limits enhancement of the photoreaction performance. With increasing temperature, the product desorption rate increases and more active sites are released. Therefore, efficient electronic transmission and utilization are crucial for this reaction. The addition of Ag to Au is beneficial for electron transfer [46]; thus, bimetal loading should enhance the photocatalytic activity compared with monometal loading and TS-1. In Fig. 11, the performance of the Au/Ag (4/1) bimetallic catalyst is consistent with the above analysis. However, with increasing Ag content in the bimetal, the photocatalytic activity decreased, which can be explained by the chemical properties and particle size of the bimetal. As previously mentioned, the physical and chemical properties of the bimetal are affected by the introduction of Ag to Au [26,27,46]. In addition, the particle size is an important factor in the photocatalytic reaction. Although the addition of Ag is beneficial for this reaction, the metal particle size (Table 1) greatly increased from 2.1 to 4.2 nm with increasing Ag content, which is adverse for the reaction [21–23]. The catalytic activity has the trend $4/1(\text{Au/Ag}) > 1/0 > 1/1 > 2/3 > 0/1 > \text{TS-1}$. For an Au/Ag mass ratio of 4/1, the highest reaction rate (68.3 $\mu\text{mol/g}\cdot\text{h}$) is attained, which is higher than the rates previously reported for Au/TiO₂ and Au/TS-1 [55]. The fact that the particle size becomes large for all the photocatalysts containing Ag suggests that aggregation occurred during the calcination process. Table 3 demonstrates that monometal or bimetal loading enhances the selectivity to PO compared with that of pristine TS-1. The optimal selectivity to PO below 363 K was reached for Au/Ag = 1/1 and was higher than that achieved with monometallic modification. Above 363 K, the selectivity of the bimetal was equivalent to that of the monometal. In other words, the bimetal plays an essential role in determining the formation rate, selectivity of PO, and product distribution.

3.3. Proposed reaction mechanism on Au/Ag-TS-1 photocatalysts

It is well-documented that tetrahedrally coordinated Ti(IV) within the framework of TS-1 plays a critical role in the photocatalytic epoxidation of propylene. As previously discussed, the UV-vis and XPS results suggest that Ti oxides were mainly dispersed in the microporous materials as isolated tetrahedrally coordinated metal oxides. The structures were reported to be easily excited under UV-light irradiation to reach the corresponding charge-transfer excited state, which includes electron transfer from O_2^- to Ti^{4+} species [56]:



Murata et al. [56] proposed that O_2 , rather than C_3H_6 , was activated on the charge transferred ($\text{Ti}^{3+}-\text{O}_L^-$) radical pair. They concluded that the active oxygen species for PO production was an electrophilic $\text{O}_3^-(\text{O}_2^+ \dots \text{O}_L^{2-})$ species generated on the photoformed hole center [56,57]. Because the photoinduced electron in Ti^{3+} is consumed by molecular oxygen ($\text{Ti}^{3+} + \text{O}_2 \rightarrow \text{Ti}^{4+} + \text{O}_2^-$), the oxidation state of Ti^{4+} is actually constant in the presence of oxygen. The generated active species (O_2^-) and (O_3^-) were thought to react with C_3H_6 to generate PO and its co-products [58]. According to the above analysis, the UV-light

excitation and photo-epoxidation processes are suitable for our photocatalytic system.

Au binds oxygen very weakly, and oxygen activation is generally thought to be a rate-limiting step for most oxidation reactions catalyzed by Au nanoparticles [59–61]. Kondarides et al. [62] observed that Au and Ag bimetal facilitated oxygen adsorption by decreasing the activation energy for molecular oxygen adsorption. Wang et al. [46] also proposed that O_2^- formation via dioxygen activation on Au–Ag was more facile than on Ag alone. Sandoval et al. [52] proposed that the bimetal easily adsorbed and activated oxygen with the change of the electronic and geometric structure of Au-based catalysts with the introduction of Ag atoms. In addition, the difficulty of electron transfer on the Au(111) surface because of its high work function [63] was alleviated by the modified electronic properties of Au with the introduction of Ag as a powerful electron donor. Therefore, a greater tendency for electron transfer between the support and bimetal is achieved, as demonstrated by the UV-vis and XPS analyses. The PL spectra also confirmed that the bimetal inhibits the recombination of photoinduced electrons and holes. Therefore, the Au–Ag bimetal provides a synergistic effect for this photoreaction. In addition, the epoxidation reaction is also connected to the reaction temperature. For the low-temperature period, product desorption is inhibited, which occupies more active sites, leading to limited photo-generated electron utilization. Therefore, the synergistic effect of bimetal catalysts is limited. With increasing temperature, more active sites are released, and the bimetal results in an obvious synergistic effect (Fig. 11), which is explained by the improved reactant adsorption, activation, and separation of photoinduced electrons and holes resulting from the introduction of the bimetal. In our photocatalytic system, the surface plasmon resonance effect of metals (Au, Ag) was easily induced under light excitation ($\lambda = 200\text{--}600\text{ nm}$) and was favorable for propylene epoxidation. The reaction mechanism could be explained by the excited electrons of the metal reacting with O_2 directly or transferring from the metal to TS-1 and then participating in the reaction. Based on these findings, we propose a mechanism for the photo-epoxidation of propylene over Au–Ag/TS-1 photocatalysts, as illustrated in Fig. 13. Under UV-light irradiation, the generated electrons and holes are

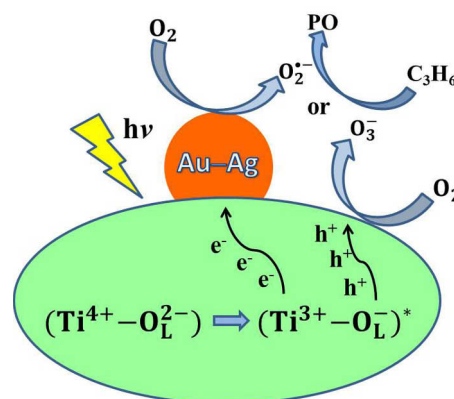


Fig. 13. Proposed mechanism for the synergistic photo-epoxidation of propylene over Au–Ag/TS-1 photocatalysts.

captured by O_2 to produce O_3^- and O_2^- active species, which react with C_3H_6 to generate PO and other by-products. During the photo-epoxidation, the Au/Ag mass ratio and reaction temperature greatly affect the catalytic activity and selectivity.

In this study, direct photo-epoxidation of propylene with O_2 was studied as a potential method for the green production of PO. This is the first time that Au–Ag bimetal has been used for the photo-epoxidation of propylene. Although some improvement of the catalytic activity was achieved for photocatalytic epoxidation, the results remain far from those needed for large-scale production. Therefore, the development of new photocatalyst systems is needed to further improve the photo-epoxidation.

4. Conclusions

Au–Ag-supported TS-1 materials were prepared using a facile two-step method, and the resulting materials were characterized using nitrogen adsorption, XRD, XPS, UV-vis, PL, SEM, and TEM and served as catalysts for propylene epoxidation. Compared with the monometallic catalytic activity, those of the bimetals showed unusual activity profiles as a function of composition and temperature. It was suggested that the addition of Ag promoted the adsorption and activation of oxygen by decreasing the activation energy for molecular adsorption of oxygen. In addition, the bimetals showed an excellent ability to transfer electrons between the support and bimetal and inhibited the recombination of photoinduced electrons and holes. A mechanism was proposed to explain this behavior, in which the alternatively intimate contact between Au and Ag provides synergism for activating O_2 and propylene, resulting in a strongly synergistic effect for propylene epoxidation. The best-performing Au–Ag bimetallic catalyst had a nominal

Au/Ag mass ratio of 4:1.

References

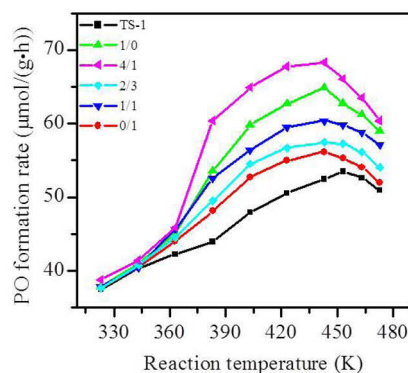
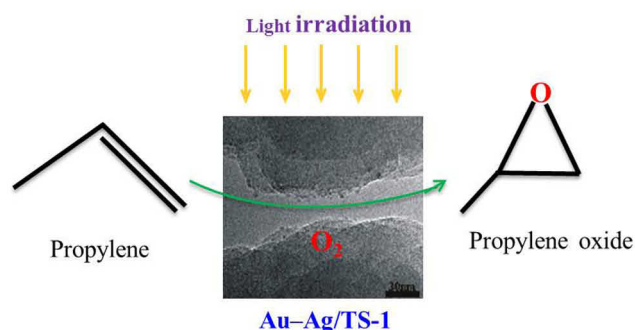
- [1] D. L. Trent, *Kirk-Othmer Encyclopedia of Chemical Technology*, John Wiley & Sons, Inc., **2000**.
- [2] T. A. Nijhuis, M. Makkee, J. A. Moulijn, B. M. Weckhuysen, *Ind. Eng. Chem. Res.*, **2006**, 45, 3447–3459.
- [3] Z. H. Suo, M. S. Jin, J. Q. Lu, Z. B. Wei, C. Li, *J. Nat. Gas. Chem.*, **2008**, 17, 184–190.
- [4] G. J. Jin, G. Z. Lu, Y. L. Guo, Y. Guo, J. S. Wang, X. H. Liu, *Catal. Today*, **2004**, 93–95, 173–182.
- [5] F. Amano, T. anaka, T. Funabiki, *Langmuir*, **2004**, 20, 4236–4240.
- [6] T. Tanaka, H. Nojima, H. Yoshida, H. Nakagawa, T. Funabiki, S. Yoshida, *Catal. Today*, **1993**, 16, 297–307.
- [7] C. Murata, H. Yoshida, J. Kumagai, T. Hattori, *J. Phys. Chem. B*, **2003**, 107, 4364–4373.
- [8] H. Yoshida, T. Shimizu, C. Murata, T. Hattori, *J. Catal.*, **2003**, 220, 226–232.
- [9] H. Yoshida, T. Tanaka, M. Yamamoto, T. Yoshida, T. Funabiki, S. Yoshida, *J. Catal.*, **1997**, 171, 351–357.
- [10] J. L. He, Q. G. Zhai, Q. H. Zhang, W. P. Deng, Y. Wang, *J. Catal.*, **2013**, 299, 53–66.
- [11] M. Haruta, B. S. Uphade, S. Tsubota, A. Miyamoto, *Res. Chem. Intermed.*, **1998**, 24, 329–336.
- [12] Y. A. Kalvachev, T. Hayashi, S. Tsubota, M. Haruta, *Stud. Surf. Sci. Catal.*, **1997**, 110, 965–972.
- [13] Y. A. Kalvachev, T. Hayashi, S. Tsubota, M. Haruta, *J. Catal.*, **1999**, 186, 228–233.
- [14] B. S. Uphade, S. Tsubota, T. Hayashi, M. Haruta, *Chem. Lett.*, **1998**, 1277–1278.
- [15] B. S. Uphade, M. Okumura, S. Tsubota, M. Haruta, *Appl. Catal. A*, **2000**, 190, 43–50.
- [16] B. S. Uphade, M. Okumura, N. Yamada, S. Tsubota, M. Haruta, *Stud. Surf. Sci. Catal.*, **2000**, 130, 833–838.

Graphical Abstract

Chin. J. Catal., 2017, 38: 831–844 doi: 10.1016/S1872-2067(17)62832-8

Synergetic photo-epoxidation of propylene with molecular oxygen over bimetallic Au–Ag/TS-1 photocatalysts

Naixu Li, Bin Yang, Ming Liu, Yong Chen, Jiancheng Zhou*
Southeast University; Southeast University Chengxian College



Au–Ag/TS-1 bimetallic catalysts prepared using a hydrothermal-immersion method showed a synergetic effect for photo-epoxidation of propylene using O_2 as the oxidant.

- [17] B. S. Uphade, Y. Yamada, T. Akita, T. Nakamura, M. Haruta, *Appl. Catal. A*, **2001**, 215, 137–148.
- [18] B. S. Uphade, T. Akita, T. Nakamura, M. Haruta, *J. Catal.*, **2002**, 209, 331–340.
- [19] E. E. Stangland, K. B. Stavens, R. P. Andres, W. N. Delgass, *J. Catal.*, **2000**, 191, 332–347.
- [20] E. E. Stangland, K. B. Stavens, R. P. Andres, W. N. Delgass, *Stud. Surf. Sci. Catal.*, **2000**, 130, 827–832.
- [21] M. S. Chen, D. W. Goodman, *Science*, **2004**, 306, 252–255.
- [22] M. Haruta, *Chem. Rec.*, **2003**, 3, 75–87.
- [23] H. Falsig, B. Hvolbæk, I. S. Kristensen, T. Jiang, T. Bligaard, C. H. Christensen, J. K. Nørskov, *Angew. Chem. Int. Ed.*, **2008**, 120, 4913–4917.
- [24] Y. Wang, J. M. Zheng, K. Fan, W. L. Dai, *Green Chem.*, **2011**, 13, 1644–1647.
- [25] C. L. Bracey, P. R. Ellis, G. J. Hutchings, *Chem. Soc. Rev.*, **2009**, 38, 2231–2243.
- [26] H. Häkkinen, S. Abbet, A. Sanchez, U. Heiz, U. Landman, *Angew. Chem. Int. Ed.*, **2003**, 42, 1297–1300.
- [27] A. M. Venezia, L. F. Liotta, G. Pantaleo, V. LaParola, G. Deganello, A. Beck, Z. Koppány, K. Frey, D. Horváth, L. Guzzi, *Appl. Catal. A*, **2003**, 251, 359–368.
- [28] X. Y. Liu, A. Q. Wang, X. D. Wang, C. Y. Mou, T. Zhang, *Chem. Commun.*, **2008**, 3187–3189.
- [29] X. Y. Liu, Y. N. Li, J. W. Lee, C. Y. Hong, C. Y. Mou, B. W. L. Jang, *Appl. Catal. A*, **2012**, 439–440, 8–14.
- [30] A. B. Smetana, K. J. Klabunde, C. M. Sorensen, A. A. Ponce, B. Mwale, *J. Phys. Chem. B*, **2006**, 110, 2155–2158.
- [31] P. G. N. Mertens, P. Vandezande, X. P. Ye, H. Poelman, I. F. J. Vankelecom, D. E. De Vos, *Appl. Catal. A*, **2009**, 355, 176–183.
- [32] J. H. Liu, A. Q. Wang, Y. S. Chi, H. P. Lin, C. Y. Mou, *J. Phys. Chem. B*, **2005**, 109, 40–43.
- [33] Y. Iizuka, A. Kawamoto, K. Akita, M. Daté, S. Tsubota, M. Okumura, M. Haruta, *Catal. Lett.*, **2004**, 97, 203–208.
- [34] A. Sandoval, A. Aguilar, C. Louis, A. Traverse, R. Zanella, *J. Catal.*, **2011**, 281, 40–49.
- [35] X. Yang, D. Chen, S. J. Liao, H. Y. Song, Y. W. Li, Z. Y. Fu, Y. L. Su, *J. Catal.*, **2012**, 291, 36–43.
- [36] R. P. Doherty, J. M. Krafft, C. Méthivier, S. Casale, H. Remita, C. Louis, C. Thomas, *J. Catal.*, **2012**, 287, 102–113.
- [37] A. Wittstock, V. Zielasek, J. Biener, C. M. Friend, M. Bäumer, *Science*, **2010**, 327, 319–322.
- [38] L. V. Moskaleva, S. Rohe, A. Wittstock, V. Zielasek, T. Kluner, K. M. Neyman, M. Baumer, *Phys. Chem. Chem. Phys.*, **2011**, 13, 4529–4539.
- [39] R. B. Khomane, B. D. Kulkarni, A. Paraskar, S. R. Sainkar, *Mater. Chem. Phys.*, **2002**, 76, 99–103.
- [40] J. W. Zheng, H. Q. Lin, Y. N. Wang, X. L. Zheng, X. P. Duan, Y. Z. Yuan, *J. Catal.*, **2013**, 297, 110–118.
- [41] V. H. Nguyen, H. Y. Chan, J. C. S. Wu, H. Bai, *Chem. Eng. J.*, **2012**, 179, 285–294.
- [42] T. Armaroli, F. Milella, B. Notari, R. J. Willey, G. Busca, *Top. Catal.*, **2001**, 15, 63–71.
- [43] E. Duprey, P. Beaunier, M. A. Springuel-Huet, F. Bozon-Verduraz, J. Fraissard, J. M. Manoli, J. M. Brégeault, *J. Catal.*, **1997**, 165, 22–32.
- [44] B. Notari, *Adv. Catal.*, **1996**, 41, 253–334.
- [45] E. Duprey, P. Beaunier, M. A. Springuel-Huet, E. Bozon-Verduraz, J. Fraissard, J. M. Manoli, J. M. Bregeault, *J. Catal.*, **1997**, 165, 22–32.
- [46] A. Q. Wang, J. H. Liu, S. D. Lin, T. S. Lin, C. Y. Mou, *J. Catal.*, **2005**, 233, 186–197.
- [47] A. Zecchina, S. Bordiga, G. Spoto, L. Marchese, G. Petrini, G. Leofanti, M. Padovan, *J. Phys. Chem.*, **1992**, 96, 4985–4990.
- [48] G. N. Vayssilov, *Catal. Rev. Sci. Eng.*, **1997**, 39, 209–251.
- [49] Z. J. Cheng, W. X. Sheng, *Chin. J. Chem.*, **2000**, 18, 42–48.
- [50] S. Bordiga, A. Damin, G. Berlier, F. Bonino, G. Ricchiardi, A. Zecchina, C. Lamberti, *Int. J. Mol. Sci.*, **2001**, 2, 167–182.
- [51] M. C. Capel-Sanchez, J. M. Campos-Martin, J. L. G. Fierro, M. P. de Frutos, A. P. Polo, *Chem. Commun.*, **2000**, 10, 855–856.
- [52] A. Sandoval, A. Aguilar, C. Louis, A. Traverse, R. Zanella, *J. Catal.*, **2011**, 281, 40–49.
- [53] T. W. Kim, M. J. Lee, *J. Adv. Eng. Technol.*, **2010**, 3, 193–198.
- [54] V. H. Nguyen, J. C. S. Wu, H. Bai, *Catal. Commun.*, **2013**, 33, 57–60.
- [55] V. H. Nguyen, H. Y. Chan, J. C. Wu, *J. Chem. Sci.*, **2013**, 125, 859–867.
- [56] C. Murata, H. Yoshida, J. Kumagai, T. Hattori, *J. Phys. Chem. B*, **2003**, 107, 4364–4373.
- [57] C. Murata, T. Hattori, H. Yoshida, *J. Catal.*, **2005**, 231, 292–299.
- [58] V. H. Nguyen, S. D. Lin, J. C. S. Wu, *J. Catal.*, **2015**, 331, 217–227.
- [59] G. Mills, M. S. Gordon, H. Metiu, *J. Chem. Phys.*, **2003**, 118, 4198–4205.
- [60] X. Y. Deng, B. K. Min, A. Guloy, C. M. Friend, *J. Am. Chem. Soc.*, **2005**, 127, 9267–9270.
- [61] J. Guzman, S. Carrettin, A. Corma, *J. Am. Chem. Soc.*, **2005**, 127, 3286–3287.
- [62] D. I. Kondarides, X. E. Verykios, *J. Catal.*, **1996**, 158, 363–377.
- [63] H. Nakatsuji, Z. M. Hu, H. Nakai, K. Ikeda, *Surf. Sci.*, **1997**, 387, 328–341.

Page numbers refer to the contents in the print version, which include both the English version and extended Chinese abstract of the paper. The online version only has the English version. The pages with the extended Chinese abstract are only available in the print version.